SUPPLEMENTARY INFORMATION

doi:10.1038/nature14349

I. OPTICAL AND MECHANICAL DESIGN

The optomechanical crystal (OMC) studied in this work is numerically optimized for both optomechanical coupling and optical/acoustic quality factor, via finite-element method (FEM) simulation in COMSOL Multiphysics [1], according to the procedure outlined in Ref. [2]. The holes on the ends of the beam support simultaneous bandgaps for optical light with wavelengths near 1550 nm and acoustic waves with frequencies from $3-5.5$ GHz, while the variation of holes towards the center of the beam perturb the bandgaps so as to create co-localized optical and acoustic mid-gap resonances. The fundamental optical mode (Fig. S-1a) has a nominal wavelength of 1545 nm and the fundamental acoustic mode (Fig. S-1b) has a nominal resonance frequency of 5.1 GHz. The nominal optomechanical vacuum coupling rate, due predominantly to photoelastic effects, is predicted to be $g_0/2\pi = 860$ kHz. Physically, this coupling rate is the optical resonance frequency shift due to the zero-point fluctuations of the acoustic resonator.

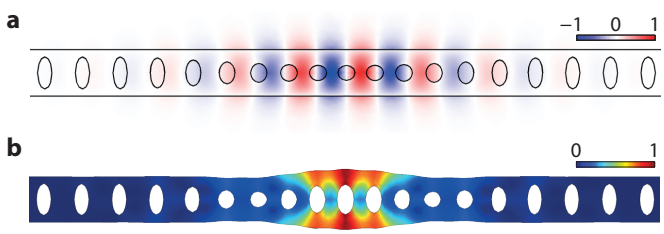

FIG. S-1: **FEM simulations. a**, Electric field E_y component of the optical mode at frequency $\omega_c/2\pi = 194$ THz (polarization in the plane of the page and transverse to the long axis of the nanobeam). **b** Displacement field of the mechanical breathing mode at frequency $\omega_m/2\pi = 5.1$ GHz.

*These authors contributed equally to this work.
†Electronic address: opainter@caltech.edu

II. FABRICATION

The devices are fabricated from a silicon-on-insulator (SOI) wafer (SOITEC, 220 nm device layer, 3μm buried oxide) using electron beam lithography followed by reactive ion etching (RIE/ICP). The Si device layer is then masked using a ProTEK PSB photoresist to define a mesa region of the chip to which a tapered lensed fiber can access. Outside of the protected mesa region, the buried oxide is removed with a plasma etch and a trench is formed in the underlying silicon substrate using tetramethylammonium hydroxide (TMAH). The devices are then released in hydrofluoric acid (49% aqueous HF solution) and cleaned in a piranha solution (3-to-1 H_2SO_4:H_2O_2) before a final hydrogen termination in diluted HF. In fabrication, arrays of the nominal design shown in Fig. S-1 are scaled by $\pm 2\%$ to account for frequency shifts due to fabrication imperfections and disorder.

III. EXPERIMENTAL SETUP

The full experimental setup for phonon counting and intensity interferometry is shown in Fig. S-2. A fiber-coupled, wavelength tunable external cavity diode laser is used as the light source, with a small portion of the laser output sent to a wavemeter (λ-meter) for frequency stabilization. The remaining laser power is sent through an electro-optic phase modulator (ϕ-m), used to generate optical sidebands for locking the filter cavities, and a variable optical attenuator (VOA) to allow control of the input power to the cavity. The signal is then sent into an optical circulator which sends the optical probe to the a lensed fiber tip for end-fire coupling to the device. The cavity reflection can then be switched to one of two detection setups. The first allows the signal to be switched to a power meter (PM) for measuring the reflected signal power or to an erbium-doped fiber amplifier (EDFA) followed by a high-speed photodetector (PD). The resulting photocurrent can be sent to a real-time spectrum analyzer (RSA) in order to measure the noise power spectral density (NPSD) of the optical signal or to a vector network analyzer (VNA) which can be used

to measure the full complex response of the optical cavity. The second detection setup sends the cavity reflection through a series of narrowband tunable Fabry-Perot filters ($\sim$ 50 MHz bandwidth, $\sim$ 20 GHz free-spectral range) in order to reject the pump frequency. The signal then travels through a variable coupler (VC) and is sent to the dilution refrigerator where it is detected by two superconducting single photon detectors (SPD). The output of these detectors is sent to a time-correlated single photon counting (TCSPC) module for calculation of the detection correlation function.

Since the pump laser is tuned to a motional sideband during the phonon counting measurement, the two Fabry-Perot filters used in this work must first be tuned to the optical cavity resonance via an initial lock and stabilization procedure. First, the pump wavelength is tuned to the blue or red OMC sideband by optimizing the mechanical transduction signal on a spectrum analyzer. Since the power of the radiated Stokes- or anti-Stokes-scattered light is too low to provide a feedback signal for filter stabilization, we then bypass the OMC and phase-modulate the pump at frequency $\omega_{\rm m}$. The filters are then locked to maximize transmission of the sideband which is resonant with the cavity. After a stabilization period of a few seconds, the filter positions are held without further feedback while the pump modulation is turned off, pump power is adjusted for the desired $n_{\rm c}$, and the OMC is switched back into the optical path. Once locked, the transmission of the filters is observed to be stable to within $5-10\%$ for several minutes in the absence of active feedback locking.

In order to avoid pile-up artifacts in the acquired $g^{(2)}(\tau)$ histograms, the photon count rate incident upon the SPDs is kept at or below 30 kHz. This is accomplished with a variable optical attenuator on the output of the filters, and is sufficient to maintain a flat histogram background over a 5 μs window. The absolute count rate reported in Fig. 3a of the main text takes the variable attenuation into account [3].

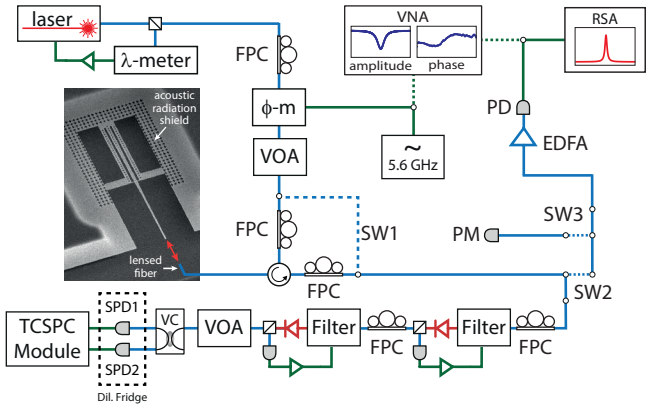

FIG. S-2: **Experimental setup.** λ-meter: wavemeter, FPC: fiber polarization controller, ϕ-m: electro-optic phase modulator, VOA: variable optical attenuator, SW: optical switch, PM: optical power meter, EDFA: erbium-doped fiber amplifier, PD: fast photodiode, RSA: real-time spectrum analyzer, VNA: vector network analyzer, VC: variable coupler, SPD: superconducting single photon detector, TCSPC: time-correlated single photon counting.

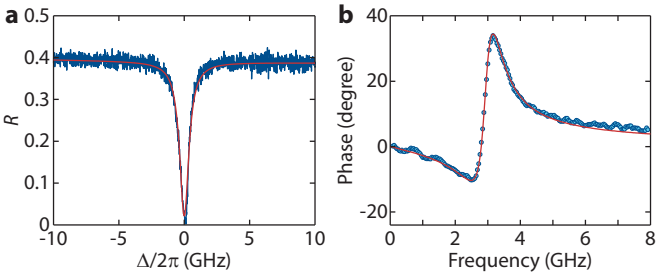

FIG. S-3: **Optical cavity response.** **a**, Optical reflection spectrum of the cavity resonance versus cavity detuning $\Delta = \omega_{\rm c} - \omega_{\rm l}$ (blue) with a Lorentzian fit (red) yielding $Q_{\rm c} = 236,000$. **b**, Phase response of the optical resonance, yielding $\kappa_{\rm e}/\kappa = 0.52$.

IV. DEVICE CHARACTERIZATION

Full characterization of the optical resonance involves determination of the single pass fiber-to-waveguide coupling efficiency $\eta_{\rm cpl}$, the total energy decay rate κ, and the waveguide-cavity coupling efficiency $\eta_\kappa = \kappa_{\rm e}/\kappa$ ($\kappa_{\rm e}$ is the decay rate into the detection channel). The fiber collection efficiency is determined by observing the calibrated reflection level far-off resonance with the cavity and is found to be $\eta_{\rm cpl} = 0.63$. The total cavity decay rate is determined by fitting the optical reflection spectrum of the cavity (Fig. S-3a) and yields $\kappa/2\pi = 818$ MHz (optical quality factor $Q_{\rm c} = 236,000$). The reflection level on resonance, when normalized to the off-resonance reflection level, is related to the cavity-waveguide coupling efficiency by $R_0 = (1-2\eta_\kappa)^2$. However, for single-sided coupling this is not a single-valued function of the coupling efficiency. Consequently, the complex response of the cavity is measured by locking the laser off-resonance from the cavity and using a vector network analyzer (VNA) to drive an electro-optic modulator (EOM) and sweep an optical sideband across the cavity. By detecting the reflected power on a high-speed photodetector connected to the VNA input, the phase response of the cavity can be measured (Fig. S-3b). Fitting this with prior knowledge of the cavity resonance frequency and decay rate yields $\eta_\kappa = 0.52$.

To characterize the acoustic resonance, the cavity reflection is sent through an erbium-doped fiber amplifier (EDFA) and detected on a high-speed photodetector. The EDFA is used to amplify the signal so that the optical noise floor overcomes the detector's electronic noise, and the noise power spectral density (NPSD) of the optical reflection is measured on a real-time spec-

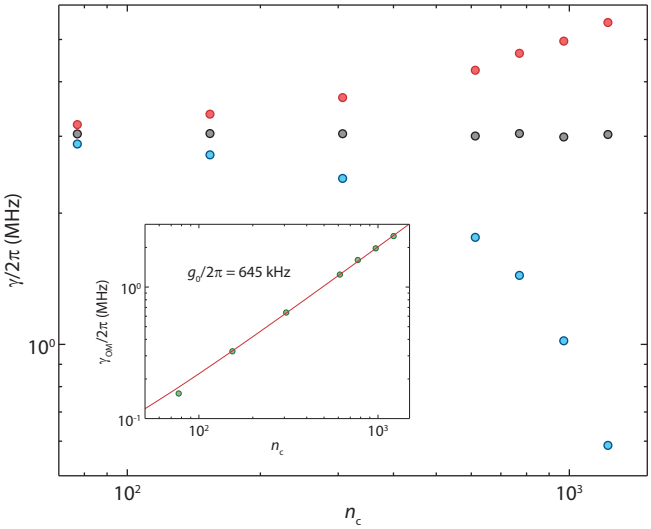

FIG. S-4: **Calibration of g_0.** Mechanical linewidth γ versus intracavity photon number n_c for $\Delta = \omega_m$ (red) and $\Delta = -\omega_m$ (blue). The intrinsic linewidth of the acoustic resonator γ_i (black) is determined by averaging the blue detuned data and yields $Q_m = 1850$. The inset shows the optomechanically induced damping γ_{OM}, obtained by subtracting γ_i from γ, versus n_c. The linear fit shown in red yields a vacuum optomechanical coupling rate of $g_0 = 645$ kHz.

trum analyzer (RSA), where a Lorentzian response due to transduction of the acoustic thermal Brownian motion can be observed at the acoustic resonant frequency $\omega_m/2\pi = 5.6$ GHz. For a pump laser locked onto the red or blue mechanical sideband of the cavity ($\Delta = \omega_c - \omega_l = \pm\omega_m$) the linewidth of the transduced signal is given by $\gamma = \gamma_i \pm \gamma_{OM}$, where $\gamma_{OM} = \pm 4g_0^2 n_c/\kappa$ (n_c is the steady state intracavity photon number). The dependence of linewidth for both detunings versus n_c is shown in Fig. S-4. By averaging the two sets of data we can extract the intrinsic acoustic damping rate $\gamma_i/2\pi = 3$ MHz ($Q_m = 1850$), which is seen to remain constant as a function of n_c. By fitting the excess optomechanically induced damping γ_{OM} as a function of n_c we extract a coupling rate of $g_0 = 645$ kHz.

V. SINGLE PHOTON DETECTORS

The detectors used in this work are amorphous WSi-based superconducting nanowire single-photon detectors (SNSPDs, or SPDs hereafter) developed in collaboration between the Jet Propulsion Laboratory and NIST. The SPDs are designed for high-efficiency detection of individual photons in the wavelength range $\lambda = 1520 - 1610$ nm with maximum count rates of about 25×10^6 counts per second (c.p.s). (reset time $t_R = 40$ ns) [4] and very low dark count rates (DCRs). With the SPD in the superconducting state (below its critical temperature $T_c = 3.7$ K), a DC bias current I_b of a few microamps is maintained through the nanowire by an external current source. The operating range of the detector lies between a lower cutoff current and an upper switching current I_{sw}, above which the nanowire switches to a non-superconducting state. The choice of quiescent operating current I_b for each detector was made to roughly maximize the ratio of the quantum efficiency η_{SPD} to DCR while operating within the "plateau" region where both η_{SPD} and the DCR are nearly constant as I_b is adjusted slightly.

The SPDs are mounted on the still stage of a ^{3}He/^{4}He dilution refrigerator at 700 mK. Single-mode optical fibers (Corning SMF-28) are passed into the refrigerator through vacuum feed-throughs and coupled to the SPDs via a fiber sleeve attached to each SPD mount. Proper alignment of the incoming fiber with the 15 μm $\times$ 15 μm square area of the SPD nanowire is ensured by a self-aligned mounting system incorporated into the design of the SPD [4]. The radio-frequency output of each SPD is amplified by a cold-amplifier mounted on the 50 K stage of the refrigerator as well as a room-temperature amplifier, then read out by a triggered PicoQuant PicoHarp 300 time-correlated single photon counting module. The counting module is triggered by input pulses reaching a voltage above a fixed discriminator value V_d. Amplified photon-detection pulse heights of $150 - 250$ mV are typical, and corresponding discriminator values in the range $110 - 150$ mV were chosen for each SPD by measuring nominal count rates as a function of V_d and choosing an operating value of V_d to be near the center of the plateau region in which the observed count rates are independent of small changes in the discriminator setting.

Initial characterization of the SPDs was centered on measuring dark count rates and the quantum efficiencies of the detectors. The measured DCRs are sensitive to various channels by which stray light may couple into the fiber-detector system, including ambient laboratory lighting and thermal radiation both inside and outside the refrigerator. By tightly spooling (~ 1.5 inch diameter) the optical fiber within the fridge to filter out long wavelength blackbody radiation and systematically isolating the optical fiber from environmental light sources we have achieved DCRs of $2 - 4$ c.p.s.

Quantum efficiency measurements of the SPDs were made using laser light of $\lambda = 1554$ nm attenuated to an input power of 1.53 fW at the input to the fridge, corresponding to $N \approx 12,000$ incoming photons per second. We calculate η_{SPD} by referring the detected photon count rate (less the corresponding known DCR) to the nominal input flux N. This efficiency incorporates the intrinsic detection efficiency of the SPDs as well as any losses in the fiber run within the fridge and in the coupling between the fiber and the SPD itself. At just below the respective switching currents of the detectors, we find $\eta_{SPD} = 70\%$, with this result depending on photon polarization ($\lesssim 20\%$ variability).

VI. PHONON COUNTING SENSITIVITY

For sufficiently weak optomechanical coupling ($g_0 \ll \kappa$) and small mechanical amplitude, the equations of motion for the optomechanical system can be linearized about a large steady state optical field amplitude. For a sideband resolved system ($\kappa/2 \ll \omega_\mathrm{m}$) and a red-detuned pump ($\Delta \approx \omega_\mathrm{m}$) the output optical field may then be written in the Fourier domain (in a frame rotating at the pump frequency), under the rotating-wave approximation, as [5]

$$\begin{aligned}\hat{a}_\mathrm{out}(\omega) &= \left(1 - \frac{\kappa_\mathrm{e}}{i(\Delta-\omega)+\kappa/2}\right)\hat{a}_\mathrm{in}(\omega) \\ &\quad - \frac{\sqrt{\kappa_\mathrm{e}\kappa_\mathrm{i}}}{i(\Delta-\omega)+\kappa/2}\hat{a}_\mathrm{i}(\omega) \\ &\quad - i\frac{\sqrt{\kappa_\mathrm{e} n_\mathrm{c}}g_0}{i(\Delta-\omega)+\kappa/2}\hat{b}(\omega), \end{aligned} \tag{S-1}$$

where $\hat{a}_\mathrm{in}(\omega) = \alpha\delta(\omega) + \hat{a}_\mathrm{vac}(\omega)$ (α is the steady-state optical field at the pump frequency, $\hat{a}_\mathrm{vac}(\omega)$ is the vacuum noise of the pump), $\kappa_\mathrm{i} = \kappa - \kappa_\mathrm{e}$ is the intrinsic loss rate of the optical cavity, $\hat{a}_\mathrm{i}(\omega)$ is additional vacuum noise admitted via the intrinsic loss channels, and $\hat{b}(\omega)$ is the annihilation operator for the acoustic resonator. Note that $\hat{b}^\dagger(\omega)$ takes the place of $\hat{b}(\omega)$ for a blue-detuned pump ($\Delta \approx -\omega_\mathrm{m}$). In general there will be a small correction to $\hat{a}$ due to the counter-rotating terms in the interaction ($\hat{b}^\dagger$ or $\hat{b}$ for $\Delta = \pm\omega_\mathrm{m}$, respectively). However, this term will be reduced by the sideband resolution ratio $\kappa/2\omega_\mathrm{m}$, and thus its contribution to any photon counting measurements will scale as $(\kappa/2\omega_\mathrm{m})^2$. As this quantity is less than 1% for our system these terms can be safely neglected.

As $\hat{b}(\omega)$ is sharply peaked around $\omega = \omega_\mathrm{m}$, we can spectrally filter out the strong optical pump at $\omega = 0$. The additional optical noise, assumed to be white Gaussian noise, cannot be filtered out in this way. However, in the case that the optical noise is pure vacuum noise it will not contribute to any photon counting events. Thus, for the purposes of photon counting the output optical field can be written post-filtering as

$$\hat{a}_\mathrm{out}(t) \approx \frac{2\sqrt{\kappa_\mathrm{e} n_\mathrm{c}}g_0}{\kappa}\hat{b}(t) = \sqrt{\frac{\kappa_\mathrm{e}}{\kappa}}\sqrt{|\gamma_\mathrm{OM}|}\hat{b}(t), \tag{S-2}$$

which shows explicitly that in this linearized regime photon counting is equivalent to phonon counting ($\langle \hat{a}^\dagger_\mathrm{out}\hat{a}_\mathrm{out}\rangle \propto \langle \hat{b}^\dagger\hat{b}\rangle$).

As can be seen in the above equation, the optically induced acoustic damping rate γ_OM physically represents the per-phonon rate of sideband photon emission, corresponding to phonon absorption (emission) for $\Delta = \omega_\mathrm{m}$ ($\Delta = -\omega_\mathrm{m}$). Of the sideband photons emitted into the optical cavity, a fraction κ_e/κ are subsequently emitted into the detection channel and detected with overall system efficiency η, including both the system efficiency of the SPDs as well as insertion loss along the path from cavity to detector. The count rate per phonon is thus given by $\Gamma_\mathrm{SB,0} = \eta(\kappa_\mathrm{e}/\kappa)\gamma_\mathrm{OM}$, and the total count rate is given by

$$\Gamma_\mathrm{tot} = \Gamma_\mathrm{SB,0}\langle n\rangle + \Gamma_\mathrm{pump} + \Gamma_\mathrm{dark}, \tag{S-3}$$

where $\langle n\rangle$ is the average phonon occupancy of the acoustic resonator, Γ_pump is the count rate due to residual pump transmission through the filters, and Γ_dark is the intrinsic dark count rate of the SPD.

To assess the sensitivity of the phonon counting measurement, the noise count rate can be divided by the per-phonon sideband count rate to obtain a noise-equivalent phonon number

$$n_\mathrm{NEP} = n_\mathrm{pump} + n_\mathrm{dark} = \frac{\Gamma_\mathrm{pump}}{\Gamma_\mathrm{SB,0}} + \frac{\Gamma_\mathrm{dark}}{\Gamma_\mathrm{SB,0}}. \tag{S-4}$$

The dark count rate Γ_dark is simply a measured constant, while $\Gamma_\mathrm{pump} = \eta A \dot{N}_\mathrm{pump}$, where A is the transmission of the filters at the pump frequency relative to the peak transmission, and $\dot{N}_\mathrm{pump}$ is the input photon flux of the pump, which is nearly perfectly reflected from the cavity when the pump is far off-resonance. For a pump detuning from the cavity of $\Delta = \omega_\mathrm{m}$, the input photon flux can be related to the intracavity photon number n_c by $\dot{N}_\mathrm{pump} \approx \omega_\mathrm{m}^2 n_\mathrm{c}/\kappa_\mathrm{e}$. Thus, we can write the total noise-equivalent phonon number as

$$n_\mathrm{NEP} = \frac{\kappa^2\Gamma_\mathrm{dark}}{4\eta\kappa_\mathrm{e}g_0^2 n_\mathrm{c}} + A\left(\frac{\kappa\omega_\mathrm{m}}{2\kappa_\mathrm{e}g_0}\right)^2. \tag{S-5}$$

VII. OSCILLATION AMPLITUDE ABOVE THRESHOLD

The classical equation of motion for the optical cavity field α is given in the frame rotating at the pump frequency by

$$\dot{\alpha} = -\left(i\left(\Delta + g_0 x\right) + \frac{\kappa}{2}\right)\alpha + \Omega, \tag{S-6}$$

where x is the position of the acoustic resonator, $\Omega = \sqrt{\kappa_\mathrm{e}P_\mathrm{in}/\hbar\omega_\mathrm{c}}$, and P_in is the optical input power at the device. In the regime of parametrically driven self-oscillation, the amplitude of the acoustic oscillator can become large enough that the usual linearization approximation becomes invalid. However, using the ansatz that the mechanical oscillation amplitude is given by $x(t) = \beta\sin(\omega_m t)$ (note that β is given in units of the zero-point amplitude, so that $\beta^2 = 4\langle n\rangle + 2$), an exact solution for the optical cavity field can be written as a sum of sidebands [6, 7].

In particular, the equation of motion can be formally integrated to yield

$$\alpha(t) = \Omega e^{-iz\cos(\omega_{\rm m}t)} \int_0^\infty d\tau e^{-\left(i\Delta+\frac{\kappa}{2}\right)\tau} e^{iz\cos(\omega_{\rm m}(t-\tau))}, \tag{S-7}$$

where $z = g_0\beta/\omega_{\rm m}$. This can be solved exactly by using the Jacobi-Anger expansion $e^{iz\cos(\theta)} = \sum_n i^n J_{\rm n}(z)e^{in\theta}$, where $J_{\rm n}$ is a Bessel function of the first kind, to yield

$$\begin{aligned}\alpha(t) &= e^{-iz\cos(\omega_{\rm m}t)} \sum_n e^{in\omega_{\rm m}t} \frac{i^n \Omega J_{\rm n}(z)}{\kappa/2 + i(\Delta + n\omega_{\rm m})} \\ &= \sum_n \sum_m e^{i(n-m)\omega_{\rm m}t} \frac{i^{n-m}\Omega J_{\rm n}(z) J_{\rm m}(z)}{\kappa/2 + i(\Delta + n\omega_{\rm m})},\end{aligned} \tag{S-8}$$

which can be re-indexed to have the form $\alpha(t) = \sum_n \alpha_n e^{in\omega_{\rm m}t}$, with

$$\alpha_{\rm n} = i^n \Omega \sum_m \frac{J_{\rm m}(z) J_{\rm m\text{-}n}(z)}{h_{\rm m}}, \tag{S-9}$$

where $h_{\rm m} = \kappa/2 + i(\Delta + m\omega_{\rm m})$. Note that if we are only interested in the total energy in the cavity, $|\alpha(t)|^2$, the final expansion of the global phase factor in Eqn. S-8 is unnecessary and a simpler form for $\alpha_{\rm n}$ involving no sums may be used [6, 7]. However, for the case considered here where a specific frequency component of the cavity output is filtered before detection it is necessary to use the full expression given in Eqn. S-9. As detailed in Refs. [6] and [7], in the regime of self-oscillation the oscillation amplitude β is determined by balancing the optically induced mechanical gain with the intrinsic mechanical loss

$$\gamma_{\rm OM} = \frac{4g_0^2\Omega^2}{\omega_{\rm m}} {\rm Im}\left[\sum_{\rm n} \frac{J_{\rm n}(z) J_{\rm n+1}(z)}{z h_{\rm n} h_{\rm n+1}^*}\right] = -\gamma_{\rm i}. \tag{S-10}$$

Note that while Eq. S-10 allows for an arbitrarily large nonlinearity due to radiation pressure, it assumes no additional contributions to the mechanical damping. Above threshold, as the amplitude of the resonator increases, it is possible that additional nonlinearities may kick in. While it is difficult to exclude such effects from first principles, as they are not well known or modeled in such systems, we note that the largest amplitude measured in this work is roughly $x \approx x_{\rm zpf}\sqrt{\langle n\rangle} \approx 3$ pm (roughly 30 times the thermal amplitude). This is far below the threshold ($\sim 1-10$ nm) where known mechanical nonlinearities such as the Duffing nonlinearity are typically observed to become significant in similar nanomechanical beams [8, 9]. More importantly, detailed studies of the limit cycle stability diagram for such nanobeam resonators well above threshold [10] have observed excellent agreement with the theory presented here, provided static detuning shifts due to thermo-optic effects (as discussed below) are taken into account. These factors strongly suggest that no additional nonlinearity is present in the system and Eq. S-10 is adequate to determine the oscillation dynamics.

The presence of the filters at the cavity output ensures that the SPD count rate is proportional to the number of intracavity photons in the first Stokes sideband at $\omega = \omega_{\rm l} - \omega_{\rm m}$, which is given by $n_1 = |\alpha_1|^2$. For the lowest input power, below threshold, n_1 is given by the simple linear approximation $n_1 = [(4G^2/\kappa)n_{\rm b}]/\kappa$, where $n_{\rm b} \approx 1100$ is the thermal occupancy of the mechanical resonator. Near and above threshold, n_1 can be determined from the ratio of the above and below threshold SPD count rates and the known value of n_1 below threshold. For a given input power with n_1 constrained, Eqs. S-9 and S-10, along with the condition that $|\gamma_{\rm OM}| \approx \gamma_{\rm i}$ above threshold, can be used to solve for the detuning Δ and amplitude β commensurate with the observed count rate.

For our highest input power, we find $\Delta \approx -1.067\omega_{\rm m}$ and $z \approx 0.15$. This amplitude is small enough that the linear approximation ($\alpha_1 \propto z$) is still valid. In particular, in the linear regime the relation $J_1(z) \approx z/2$ should hold. For the largest value of z in our measurements, we find that $J_1(z)$ differs from $z/2$ by only about 0.3%. Note that, while this detuning shift is comparable to the cavity linewidth, it is a static shift derived from a fully nonlinear theory and as such is not at odds with the linear response of the cavity in the limit cycle regime. The shift in detuning, and the concomitant reduction in oscillation amplitude, is expected due to the thermo-optic effect which will tend to shift the cavity resonance to lower frequencies as the total intracavity photon population is increased by the amplified Stokes scattering [10]. This thermo-optic shift has been previously observed in similar nanobeam OMC structures [11].

In the linearized regime, $n_{\rm c}$ (the intra-cavity photon number of the 0th order sideband at $\omega_{\rm l}$) is to a good approximation equal to the intra-cavity photon number in the absence of optomechanical coupling, $n_{\rm c} = (4\kappa_{\rm e}P_{\rm in}/\hbar\omega_{\rm l})/(\kappa^2 + 4\Delta^2)$. The total optomechanical back-action rate ($\gamma_{\rm OM}$) is also approximately equal to the scattering rate from the 0th sideband to the 1st Stokes sideband ($\gamma_{0,1}$) in the linearized regime, which for $\Delta = -\omega_{\rm m}$ blue detuned pumping yields $|\gamma_{\rm OM}| \approx \gamma_{0,1} \approx 4G^2/\kappa$. As this is the case, in the main text we don't differentiate between back-action damping and Stokes scattering rate, and $n_{\rm c}$ is a simple placeholder for $P_{\rm in}$ in all of our plots.

VIII. PHOTOTHERMAL EFFECTS

As described above, heating due to optical absorption plays a role in determining the operating point of the oscillator at the highest powers via thermo-optic shifts of the optical resonance frequency. This raises the question of whether or not photothermal forces also have a sub-

stantial effect on the dynamics of the oscillator at high power. The per-photon force due to radiation pressure is simply given by $F_{\rm rad} = \hbar g_0/x_{\rm zpf}$, where $x_{\rm zpf}$ is the zero-point amplitude of the mechanical resonator, calculated to be ~ 3 fm in our structure. Using our measured g_0 value, this yields a per-photon radiation pressure force of $F_{\rm rad} \approx 0.15$ pN.

The per-photon photothermal force, on the other hand, can be expressed in terms of the temperature change and thermal parameters of the cavity as [12]

$$F_{\rm pht} = D\Delta T \frac{\gamma_{\rm th}^2}{\omega_{\rm m}^2 + \gamma_{\rm th}^2}, \qquad \text{(S-11)}$$

where D is a thermo-mechanical force coefficient detailing the effective force on the resonator per unit temperature change, ΔT is the overall temperature shift of the resonator volume, and $\gamma_{\rm th}$ is the thermal decay rate. For small ΔT, the temperature shift is related to the thermo-optic shift via the relation $\Delta\omega_{\rm c}/\omega_{\rm c} = \frac{-1}{n}\frac{dn}{dT}\Delta T$. Using the known thermo-optic coefficient $\frac{dn}{dT}$ for Si at room temperature and $\lambda \approx 1550$ nm [13], we find that the largest $n_{\rm c}$ (where $\Delta\omega_{\rm c} \approx -0.067\omega_{\rm m}$) results in a temperature shift of $\Delta T \approx 0.04$ K. The thermal decay rate can be determined from the relation $\gamma_{\rm th} = G_{\rm th}/C_{\rm th}$, where $G_{\rm th}$ and $C_{\rm th}$ are the thermal conductance and heat capacity, respectively. These parameters can be determined using the known thermal conductivity, density, and specific heat of Si at room temperature, along with the geometric parameters of the resonator, to obtain $\gamma_{\rm th}/2\pi \approx 600$ kHz. The thermo-mechanical coefficient D can be roughly estimated by observing that the breathing mode predominantly involves dilatational motion along the transverse axis of the beam (see Fig. S-1b). Thus, D will be approximately given by $D \approx \alpha_{\rm th} E A_{\rm eff}$, where $\alpha_{\rm th}$ is the linear thermal expansion coefficient, E the Young's modulus, and $A_{\rm eff}$ the cross-sectional area of the mechanical mode perpendicular to the motion. Estimating D in this fashion yields $D \approx 200$ nN/K. Combining these estimates for ΔT, $\gamma_{\rm th}$ and D in Eq. S-11 yields $F_{\rm pht} \approx 0.1$ fN for the maximum input power. As this figure is more than 1000 times weaker than the radiation pressure force, we can safely neglect the possibility of additional photothermal effects.

[1] COMSOL Multiphysics 3.5, http://www.comsol.com/.

[2] J. Chan, A. H. Safavi-Naeini, J. T. Hill, S. Meenehan, and O. Painter, Appl. Phys. Lett. **101**, 081115 (2012).

[3] W. Becker, *Advanced Time-Correlated Single Photon Counting Techniques* (Springer Verlag, New York, 2005).

[4] F. Marsili, V. B. Verma, J. A. Stern, S. Harrington, A. E. Lita, T. Gerrits, I. Vayshenker, B. Baek, M. D. Shaw, R. P. Mirin, et al., Nature Photon. **7**, 210 (2013).

[5] A. H. Safavi-Naeini, J. Chan, J. T. Hill, S. Gröblacher, H. Miao, Y. Chen, M. Aspelmeyer, and O. Painter, New J. Phys. **15**, 035007 (2013).

[6] F. Marquardt, J. G. E. Harris, and S. M. Girvin, Phys. Rev. Lett. **96**, 103901 (2006).

[7] D. A. Rodrigues and A. D. Armour, Phys. Rev. Lett. **104**, 053601 (2010).

[8] A. H. Nayfeh and D. T. Mook, *Nonlinear Oscillations, Physics and Applied Mathematics: A Wiley-Interscience Series of Texts, 1st ed., Monographs and Tracts* (John Wiley, 1979).

[9] X. L. Feng, C. H. White, A. Hajimiri, and M. L. Roukes, Nat. Nanotech. **3**, 342 (2008).

[10] A. G. Krause, J. T. Hill, M. Ludwig, A. H. Safavi-Naeini, J. Chan, F. Marquardt, and O. Painter, in preparation (2014).

[11] J. Chan, T. P. M. Alegre, A. H. Safavi-Naeini, J. T. Hill, A. Krause, S. Gröblacher, M. Aspelmeyer, and O. Painter, Nature **478**, 89 (2011).

[12] D. Woolf, P.-C. Hui, E. Iwase, M. Khan, A. W. Rodriguez, P. Deotare, I. Bulu, S. G. Johnson, F. Capasso, and M. Loncar, Opt. Express **21**, 7258 (2013).

[13] B. J. Frey, D. B. Leviton, and T. J. Madison, in *Proc. SPIE* (2006), vol. 6273, p. 62732J.